The Effect of Geometry on Modelling Electrical Signals in Biofilms

Harry Lipscomb

10449626

School of Physics and Astronomy

The University of Manchester

MPhys Project Report

September - December 2022

Abstract

Chemical electro-signalling allows for long-range communication between stressed bacteria in biofilms through a propagating wave of K^+ ions. An agent-based fire-diffuse-fire model was used to examine the properties of this communication in simple biofilm shapes, biofilms with channels and fractal biofilms. Superdiffusion was observed within spherical, hemispherical and cylindrical biofilms with diffusion exponents 1.54 ± 0.01, 1.69 ± 0.02 and 1.78 ± 0.01 respectively. A significant time-delay was seen in biofilms with square and circular channels that arose not only from an increase in the required propagation distance for the K^+ waves but also due to a break in the waves spherical symmetry . The latter source of delay was seen to be the dominant time-delay effect for biofilms with channels of widths 30% the biofilm diameter or less. To conclude, the Diamond-Square Algorithm was implemented to form rough surfaces of known fractal dimension. From this, it was observed that the first passage time for a wave across a rough surface was proportional to its roughness and a study into the relationship between fractal dimension and wave velocity through a range of fractal biofilms was completed.

Contents

1 Introduction

To increase tolerance to environmental stresses such as hazardous chemicals, pH fluctuations and electromagnetic stimulation, bacteria have evolved to form biofilms. These are complex communities of cells able to form on almost all surfaces [1, 2]. They are made when microbial cells are enclosed by a self-produced, extracellular polymeric substance (EPS) matrix and attach to a surface [3]. EPSs are responsible for the structure and stability of cells within the biofilm and are primarily made of polysaccharides (long chains of carbohydrate molecules) and proteins but also include DNA, lipids and humic substances [4]. The National Institute of Health states that more than 60% of microbial infections are caused by biofilms [5], many of which cause chronic and reoccurring health issues. During 2007, biofilms were responsible for over half a million deaths in the US alone [6]. Studying communication mechanisms within biofilms is therefore crucial as it may provide an important step in controlling biofilm-mediated drug resistance and offer new routes for the delivery of dispersal agents [7].

Bacteria in biofilms communicate in two ways: quorum sensing (QS) and chemical electro-signalling. QS is a close-range communication mechanism which allows bacteria to collectively alter their gene expression to maximise survival chances in response to external stress; it is the form of communication behind biofilm formation and dispersion [8]. Chemical electro-signalling allows long range communication between bacteria in a biofilm. This occurs when a spatially propagating wave of ions depolarise neighbouring cells [9] causing them to diffuse their own ions. This mechanism is discussed further in Section 2.1.

During this study, an agent-based Fire-Diffuse-Fire (FDF) model, explained in Section 3.2, was used to model electro-signalling within bacterial biofilms. Randomly generated bacteria within simple shapes, biofilms with channels and rough, fractal biofilms were stressed to investigate the way in which geometry affects this communication mechanism.

2 Theory

2.1 Communication in Biofilms

When a bacterial membrane separates two ionic concentrations of varying charge, a potential difference between the extra-cellular and intra-cellular ions is formed. This is called a Nernst Potential [10] and is an example of an action potential. An action potential is defined to be a sudden, transitory and propagating change in a systems rest potential [11]. The potential difference across a cell membrane is defined to be the intracellular potential less the extracellular potential and so is negative by convention. There are two features that govern the movement of ions across this membrane: the electrical gradient and the concentration gradient. A bacteria membrane is not always in equilibrium as it acts as a barrier to ion migration. Two transport mechanisms within cell membranes exist which allow ions to permeate: carriers (such as ion pumps) which bind to ions and transfer them across the membrane and ion channels which act as pores that can have a range of ion selectability [11].

B. subtilis and *E. coli* act as action potentials when the Nernst potential changes due to a change in extracellular charge. Consequently, the bacterial membrane moves through three states: depolarisation, hyperpolarisation and repolarisation. Depolarisation results from an influx of positive ions across the membrane whereas repolarisation and hyperpolarisation occur from an efflux of positive ions.
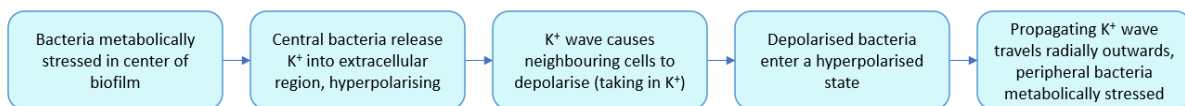

Figure 1: The key polarisation steps of a propagating, centrifugal wave due to an action potential across a bacterial membrane. The initial environmental stress is often due to competition between central and peripheral cells for nutrients like glutamate, GLU^- [12].

Prindle *et al.* showed that long-range electrical communication occurs when propagating potassium (K^+) waves travel across bacteria within a biofilm [12]. To show this, *B. subtilis* biofilms were studied as they had previously demonstrated metabolic oscillation between interior

and peripheral bacteria when experiencing nutrient limitations [13]. During the study, Thioflavin T (Tht) dye was used as a Nernstian voltage indicator. As Tht is positively charged, it is retained within the negative potential of a bacteria and thus its concentration is inversely related to membrane potential. Images from the paper are shown in Figure 2.
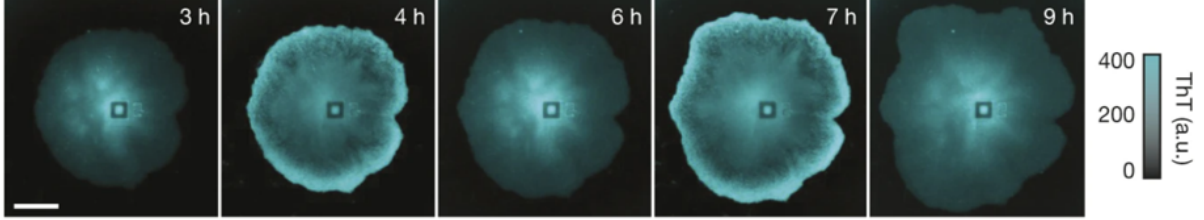

Figure 2: Global oscillations in *B. subtilis* membrane potential due to K^+ waves, observed using ThT dye [12]. This image was formed from over 75 independent biofilms. The Tht concentration is given in arbitrary units and a scale bar of 150 μm is included.

Potassium ions, the most abundant intracellular cation in all living cells [14], were shown to be the source of active signalling in the biofilm. This was demonstrated when Tht oscillations were quenched following a uniform addition of potassium chloride at the intracellular concentration - 40 times the extracellular concentration. Specifically, the Yug0 K^+ channel, regulated by the metabolic state of the cell, activated when bacteria was under a glutamate limitation, was shown to be a significant source of the potassium wave. This was shown when bacteria without the Yug0 channel did not hyperpolarise or fire under an external potassium shock.

There are several circuit-based models which swap features of a bacterial membrane with electrical components in order to mathematically reflect the membrane potentials of *B. subtilis* and *E. coli* over time. The first quantitative method to describe action potentials across a neuron was the Hodgkin-Huxley model. It has been successfully applied to a vast range of excitable cells, including bacteria [10]. During this paper, a step-function is used as a first-order approximation to the shape of the K^+ firing from a stressed bacteria. The Hodgkin-Huxley equations offer scope for development within the model used here.

2.2 Diffusion

Adolf Fick was the first to propose a quantitative, universal measure of diffusion in 1855 [15]. In his paper, he follows principles used by Fourier for the flow of heat and by Ohm towards the dissipation of electricity in a conductor. His intuition leads him to apply these concepts to the diffusion of salt in solution and propose Equation 1, Ficks (second) Law, stated as

$$\frac{\partial \phi}{\partial t} = D\nabla^2 \phi \tag{1}$$

where ϕ represents the concentration field for a substance and D is the diffusion coefficient. Equation 1 describes Fickian diffusion, an example of which is a particle undergoing Brownian motion which was considered by Einstein in 1905 [16]. Given Equation 1, $\int_R \phi(x,t)dx$ can be interpreted as the probability the particle is found within a region R at time t. The above differential equation is then solved (in one spatial dimension) by the exact solution

3

$$\phi(x,t|x_0,t_0) = \frac{1}{2\sqrt{\pi D(t-t_0)}} \exp\left(-\frac{(x-x_0)^2}{4D(t-t_0)}\right) \tag{2}$$

by assuming an initial spike: $\phi(x = x_0, t = t_0) = \delta(x)$ and that the boundary conditions are $\phi(x,t) \to 0$ as $x \to \infty$. Through the typical definition of expectation values, this solution derives Equation 3 in which the mean square displacement, $\langle r^2 \rangle$, is linearly related to the number of spatial dimensions, d and the time elapsed, τ.

$$\langle r^2 \rangle = 2dD\tau \tag{3}$$

There are many natural situations in which this linearity does not hold [17, 18] where the more general form

$$\langle r^2 \rangle \propto \tau^\alpha \tag{4}$$

fits the motion observed. In Equation 4, α is the diffusion exponent, a constant which results from the properties of the system. In the case of barriers, binding sites or any such feature which oppose free diffusion within a system, this leads to subdiffusion [18], where $\alpha < 1$. If random steps of varying length are taken by a particle [17], intrinsic motors drive a flow of some substance [19] or the diffusive substance is consistently added, as during this study, superdiffusion is observed in which $2 > \alpha > 1$. Hyper-ballistic behaviour has been observed in optical systems [20] in which $\alpha > 2$.

2.3 Defining a Wavefront

There are several ways in which the potassium wavefront, the propagating signal of interest, may be defined. Initially, the wavefront was calculated using the average concentration of K^+ within spheres of varying radius centered on the middle of the biofilm. Although this offered a complete picture of the potassium diffusing within a spherical biofilm, this definition poorly reflected the features of a wavefront propagating in any non-spherically symmetric biofilm. To compare the diffusion exponent between shapes and determine the position of the wavefront at a given time, an alternative definition was used. The wavefront was taken to be the position furthest from the initial spike where the concentration of K^+ is above a defined threshold, σ^*. A discussion of this parameter and the method by which the wavefronts were determined is in Section 3.4.

2.4 Fractal Terrains and Surface Roughness

The fractal dimension of a geometry was first introduced by Mandelbrot in 1967 to describe geographical curves such as the British coastline which had "undefinable" lengths [21]. As finer and finer features of the coastline were included in a calculation of its total length, there was no convergence to a measurable value. This lead to an alternative characterisation of naturally occurring shapes and extended conventional Euclidean descriptions in which lines, planes and

volumes have dimensionality of one, two and three respectively. The quantity devised had all the properties of a dimension, although its value was typically non-integer. The unique characteristic of these complex shapes, later coined fractals by Mandelbrot, is they follow the relation

$$M(l) \propto l^D \tag{5}$$

in which $M(l)$ can represent the volume of an object, the area of a surface or the length of a curve, D is the fractal dimension and l is some length [22]. Equation 5 implies self-similarity, the characteristic feature that fractals have similar statistical properties across a range of length scales.

Most natural objects have structural self-similarity that cannot be wholly described by Euclidean geometry [23]. Fractal dimension as a property of these objects has been studied over a vast scale in the natural world: from the membranes of biological cells [23] to crater ejecta across the solar system [24]. A further discussion of fractal dimension studies specific to biofilms is included in Section 2.5.

As well as characterising natural curves, fractal dimension can also be used as a measure of surface roughness [25]. During this study, the Diamond-Square Algorithm (DSA) was used to generate undulating, rough surfaces of varying fractal dimension. The relationship between fractal dimension and average propagation speed within several fractals was then considered. Two other roughness parameters were used to characterise the fractal terrains generated by the DSA. First, the route-mean-square (RMS) of the bacteria heights, R_{rms}, given by

$$R_{rms} = \sqrt{\frac{1}{N} \sum_{i=1}^{N} z_i(x,y)^2} \tag{6}$$

was calculated. N is the total number of bacteria on the biofilm surface and z_i is the height of the i'th bacteria. As the bacteria were generated with a mean height of zero, R_{rms} also acts a measure of the standard deviation of the bacteria heights. The kurtosis of the heights, R_{ku}, was also calculated through

$$R_{ku} = \frac{1}{R_{rms}^4} \left[\frac{1}{N} \sum_{i=1}^{N} z_i(x,y)^4 \right] \tag{7}$$

as a measure of the distributions peakedness.

2.5 Biofilm Geometry

Confocal scanning laser microscopy (CSLM), an optical imaging technique in which a pin-hole is used to block out-of-focus light in a microscope, was patented in 1955 by Marvin Minksy [26]. This offered a revolution in the 2D segmentation and sequential 3D imagining of biofilms through vast improvements in axial resolution [27].
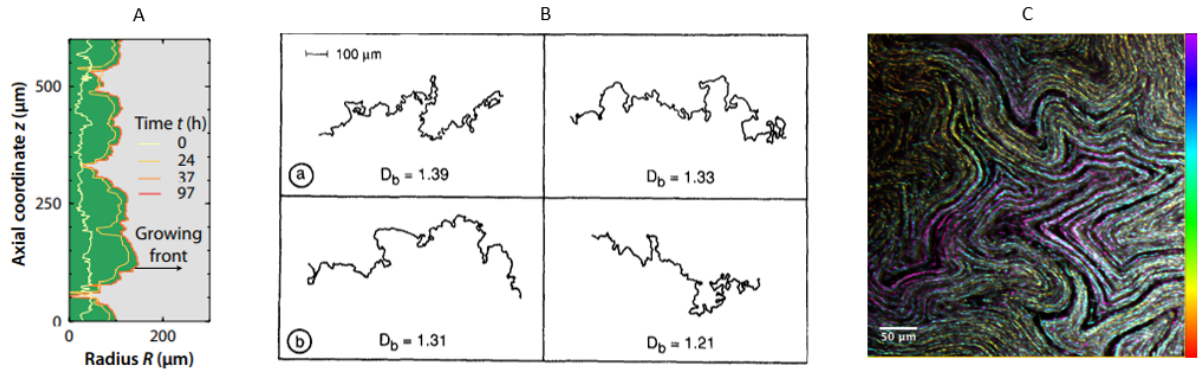
Figure 3: Three examples of the fractal geometries observed in 3D biofilms. *A* shows an *E. coli* biofilm cross-section after various time frames of growth over which a fractal-like morphology is observed on length scales of 100 to $200\,\mu m$ [28] . *B* shows surface profiles of 27-day old biofilms sampled from four compartments of a rotating biological contactor. The surface fractal dimension is found by summing two orthogonal boundary fractal dimensions, D_b, in the plane of the biofilm. *C* shows channels observed within a $36\,\mu m$ thick sub-stack of *E. coli* [7]. A colour bar shows the depth of each cell in the biofilm, where purple represents the deepest bacteria and red the shallowest.

Following the application of CSLM, biofilm structure has been well researched. Several studies propose a characteristic fractal dimension, D, for various biofilms. Schindler, Hermanowicz and Wilderer find values of $2.50 < D < 2.67$ for scales of 12 to $30\,\mu m$ within the biomass of heterotrophic, aerobic biofilms [29]. Alternatively, Zahid and Ganczarczyk find $2.1 < D < 2.8$ for biofilms on rotating biological contactors over the scale of $100\,\mu m$ [30], shown in Figure 3B.

Given the support for the characterisation of biofilm geometry through fractal dimension, one of the aims of this study is to demonstrate a process of forming and simulating biofilm surfaces of quantifiable fractal dimension within an agent-based model.

Within *E. coli*, it has been shown that intra-colony channels, with diameters on the order of $10\,\mu m$, form as an emergent property of biofilm growth [7]. This plays a role in the distribution of nutrients around the biofilm and offers an effective mechanism by which dispersal agents may be administered to biofilms. To understand the effect that channels may have on electrical signalling within a biofilm, this was explored during the study.

2.6   First Passage Time

The mean first-passage time (MFPT) is often used to define the characteristic time scale of a stochastic process. Therefore, first-passage time distributions are used within biology, physics and financial mathematics and there is a vast literature behind analytical solutions to simpler stochastic systems than the one used here. During this study, the MFPT was taken to be the average time during which the wavefront passes a predetermined position on the biofilm being simulated. Physically, this represents the length of time a stressed bacteria (at the location of the initial spike) would be able to communicate this stress to a bacteria at the predetermined location.

3 Computational Setup

3.1 Overview of BSim

An agent-based model (ABM) is a stochastic model comprised of many individual agents, in this case bacteria, that interact with their environment by a defined set of rules. The Java-based ABM BSim 2.0 [31] was used within the study to learn about macroscopic signalling across these bacteria. BSim was used as it offers a variety of bacteria properties in modular packages which includes motility, replication and chemical fields. BSim typically incorporates "run and tumble" motion observed within planktonic bacteria in sparse suspensions. Here, the bacteria show straight runs in which multiple flagella (helical, hair-like structures which act as molecular propellers) uniformly rotate in a counter-clockwise direction to generate thrust. Interspersing runs, a flagella may flip to clockwise rotation causing a random reorientation termed a tumble. The frequency of tumbles is governed by chemotaxis signalling which encodes a bacterias short-term memory and causes longer runs in nutritionally preferable directions [32].

During this study, bacteria were stationary to model high-density biofilms in which bacterial motion is low. BSims *ChemicalField* program was used to split up the large volume of interest into $1\,\mu m^3$ boxes, each with a measurable concentration of K^+. This potassium diffuses in discrete time-steps, set to one second within the model, according to Fick's laws and hence it diffuses as a function of the concentration gradient, rather than flagella rotation.

3.2 Fire-Diffuse-Fire Model

During the study, the FDF model [10] was used to model electrical signalling in bacteria. In the model, once the potassium concentration reaches a threshold value, c^*, at a (fixed) bacteria site, the bacteria fires and releases a concentration, σ, of K^+ each second. The potassium concentration in a biofilm will consequently follow the reaction-diffusion equation

$$\frac{\partial \phi}{\partial t} = D_K \frac{\partial^2 \phi}{\partial x^2} + \sigma \sum_n \delta(x - x_n)\delta(t - t_n) - k\phi \tag{8}$$

where ϕ is the concentration of K^+, D_K is the diffusion coefficient for the potassium and t_n/x_n is the time/position at which the K^+ rises above threshold for the nth bacteria site. The first term in Equation 8 arises from Fickian diffusion and the second is a firing function which contributes when the bacteria is stressed. Here, a homogeneous uptake term, $-k\phi$, is required to preserve K^+ over long time periods, in agreement with simple conservation rules. As discussed during Section 2.1, the Hodgkin-Huxley equations may be used to provide a more accurate firing shape for the bacteria. Equation 8, in this case, would then be modified to have a time-dependent function appended to the second term on the right-hand side to account for this. During this study, a rectangular firing function was used so bacteria would fire at a constant rate for a period of time. In the next section, the parameters used with the model are discussed further.

3.3 Initial Parameters

There were several parameters within BSim chosen before the simulations were run: D_K, σ, k, σ^* and the density and geometry of the bacteria. D_K, σ and σ^* were chosen to form a propagating wave which matched typical time and length scale data for electrical signalling within biofilms. σ^* is the threshold concentration above which the bacteria fire. As mentioned previously, k was an uptake rate uniformly applied to the K^+ concentration across the whole field. As conserving K^+ in the short-term was challenging given the stochastic nature of the bacteria firing patterns, the uptake parameter was set to conserve K^+ over a longer period after which the wave had propagated to the edge of the shape. The threshold for firing was set to be one order of magnitude lower than σ, the quantity added when firing. If the threshold was set significantly lower than this, the wave would propagate very quickly and require few bacteria to possess a firing mechanism. This is not observed in the literature.

BSim offers both periodic and reflective boundary conditions in which K^+ travelling towards the simulation boundary either re-enters the simulation from the opposite face or reflects off the boundary. A reflective boundary condition was chosen for the study for a clearer understanding of K^+ flow when a simple shape had one face on the simulation boundary (seen in Figure 4). For shapes such as the basic sphere and the fractal surfaces, this had little impact as the boundaries were extended to negate any edge effects. The boundary condition is best observed during the results of the cylinder with a tight boundary in Section 4.1.

Lastly, the geometry and density of the bacteria was chosen. Initially, simple shapes were investigated which included: spherical, hemispherical and cylindrical biofilms. For each, bacteria were randomly generated within the shape to form an approximately constant density within the shapes boundaries. As the diffusion exponent and MFPT for each shape was a function of bacteria density, the total number of bacteria within each shape was scaled with its volume. Hence, when changing the shape of the biofilm, only the effect of changing geometry is seen within the results. The code used to spawn the bacteria was initially implemented in Python to ensure density was constant within each shape.
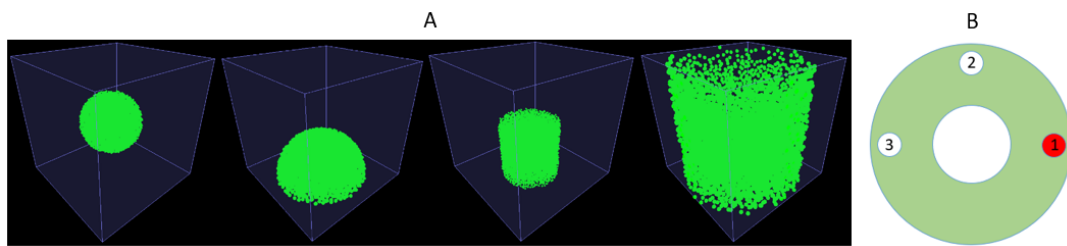

Figure 4: *A* shows all the simple shapes formed. In order, these were: spherical, hemispherical and cylindrical biofilms with both far and tight reflective boundaries. The large cube, the region of the simulation, was set to have a side length of 128 μm for all shapes except the cylinder with tight boundaries which was of side length 64 μm. The axis along which results were recorded was the central axis for all simple shapes. *B* shows the axis of interest for the circular hole study, where Axis 1 is red as it is the location of the initial spike, 3 μm from the edge of the cylinder.

Following the simple shapes study, a circular channel was added to the cylindrical biofilm and a cuboidal biofilm with a square hole through one axis was generated, once again scaling the total bacteria when the hole size was modified. Finally, rough terrains generated by the DSA and

Menger Sponges of both two and three dimensions were formed in the simulation to conclude with a study into fractal dimensions affect on signalling. A full table of the parameters used is found in Appendix A.1.

3.4   Data Collection and Uncertainties

Using BSim, the simulation for each previously mentioned geometry was completed and the concentration of K^+ within each $1\,\mu m^3$ box along axis/planes of interest was recorded to Excel files. This was read into Python where the concentrations were changed into binary to represent if each box was above or below a specified value at each given time-step. This threshold was set to be σ^* so the wavefront also reflects the time at which any bacteria in that position would fire. The outermost point of the wave was then found using a Python script.

There were two sources of uncertainty combined to form the uncertainty in the wavefront positions: the random generation of the biofilms which forms regions of minorly varying bacteria density and the discrete boxes used to determine the wavefront position at each time-step. To quantify the prior, which is the dominant uncertainty, at each time-step the standard deviation between five repeats of the wavefront position was taken. For the latter, an error of $0.5\,\mu m$, half the measurement interval, was used. Both of these errors were propagated together to provide final uncertainties on the wavefront position squared as seen in the plots of $\langle Y^2 \rangle$ in Figure 8. From Equation 4, the curve

$$\langle r^2 \rangle = K_\alpha \tau^\alpha + C \tag{9}$$

was fit to the data where K_α, C and α are all parameters whose value and uncertainty are given by the fitting.

3.5   Diamond-Square Algorithm

To create a fractal-like terrain for the biofilm, a statistically self-similar technique for surface generation is required. The best known example of statistical-similarity is the progressive increments of fractional Brownian motion (fBm). Here, if u is defined to be a real parameter, the fBm function, B_D, with self-similarity parameter H obeys Gaussian properties $\mu = 0$ and $\sigma_u^2 > 0$ [33]. Furthermore, $B_D(u + \delta u) - B_D(u)$ and $B_D(u + h\delta u) - B_D(u)$ will have the same distribution if the second expression is rescaled by h^{-D} [34].
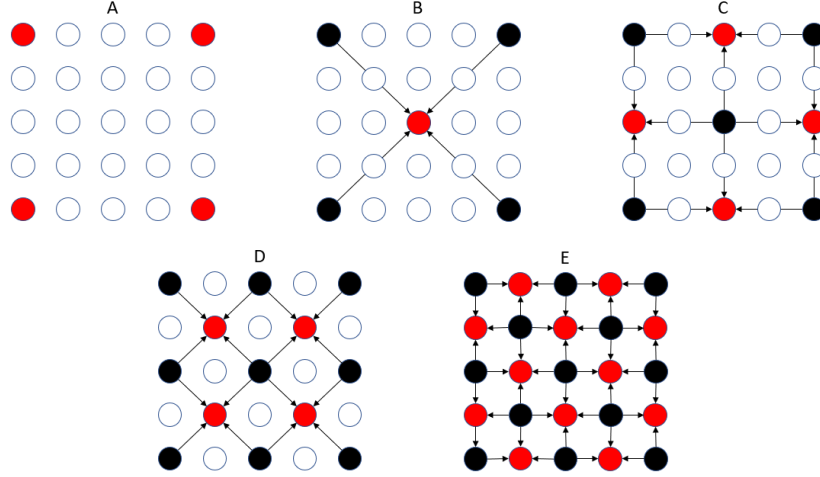
Figure 5: The Diamond-Square Algorithm used to generate fractal surfaces for a five by five lattice of bacteria. At *A*, the corner points are fixed to zero. Steps *B* and *D* demonstrate diamond steps and steps *C* and *E* show square steps. Red indicates that the point, which represents a bacteria height, is formed that step and black points are generated prior to the shown stage.

The algorithm alternates between completing diamond/square steps of diminishing scale until all points are given a value. At each of these steps, virtual diamond/squares are drawn, as shown by the arrows in Figure 5, to determine the central bacterias height from surrounding bacteria. A bacteria height, h_i, with N surrounding bacteria of height h_j, is thus calculated by

$$h_i = \frac{1}{N} \sum_{j=1}^{N} h_j + R \tag{10}$$

where R is a randomly generated number in the range $[-r, r]$. Therefore, r is used as a typical scale for the deviation between adjacent bacteria heights within the generated terrain and hence a roughness parameter which is related to fractal dimension and MFPT in Section 4.3.

The Diamond-Square Algorithm (DSA) was chosen as the surface fractal generator used within the study for two primary reasons: it is highly customisable in both the scale and roughness of the surfaces it creates and it generated self-similar terrains. Within the study, the self-similarity of the terrains generated was check by plotting the distribution of bacteria heights it formed. This is explored in Appendix A.2.
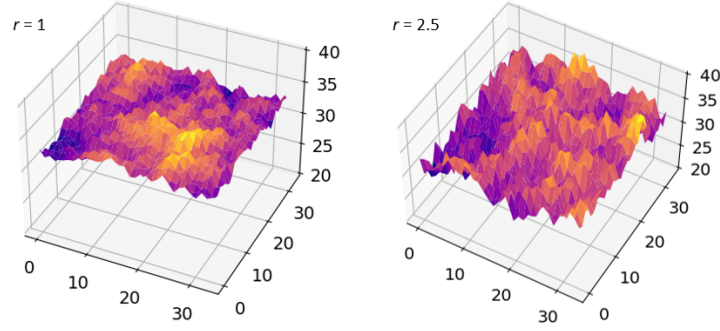
Figure 6: Two examples of surfaces formed for $r = 1$ and $r = 2.5$ on 33 by 33 μm grids using the DSA. An increase in r forms a rougher surface whilst lower r creates a smoother, undulating surface with less deviation between adjacent bacteria.

There were two limitations to the DSA when relating the surfaces generated to physical biofilms. The first was that the side lengths of the terrain had to be $2^k + 1$ boxes in length, where k is an integer, due to the way the algorithm iterates inwards from the corner values. Secondly, the bacteria viewed aerially form a lattice which does not reflect the irregularity of bacteria positions in physical biofilms. This may be resolved by placing a random offset on each bacteria as to create a more physical, random system. When trialled, this prevented BSim from running simulations as the software would not operate if two bacteria volumes overlapped.

Regardless, the DSA offered a useful approximation to a biofilm surface as the macroscopic changes in signalling caused by different surface roughnesses would be very similar if a small offset (with a mean of zero) was applied to each bacteria. An extension to the algorithm may be that bacteria are generated within a region according to a probability which is a function of the bacteria already in that region. This would lead to clumping within the biofilm in which colonies of bacteria form in locally dense regions and would reflect another physical property of biofilms.

3.6 Determining Fractal Dimension

To characterise the fractal dimension of surfaces produced by the Diamond-Square Algorithm, there are several methods available. Here, the study computes the Minkowski-Bouligand dimension, D, using a box counting method [35]. This technique was used as it was the most computationally efficient and robust given the large range of surface roughnesses formed by the fractal generating algorithm.

To determine D, an imaginary cube is formed to enclose all bacteria on the generated rough surface. This cube is then split up into smaller cubes of side length s_i. The number of these smaller cubes that enclose one or more bacteria, $N(s_i)$, is counted using a Python script. This processes is repeated for a range of cube sizes and the relation

$$\log(N(s_i)) = a - D\log(s_i) \tag{11}$$

can be fit to find the fractal dimension, where a is a constant. This is shown in Figure 7 which

provides a two dimensional example of the box counting method. Individual bacteria were taken to be infinitely small such that they could not overlap between boxes.
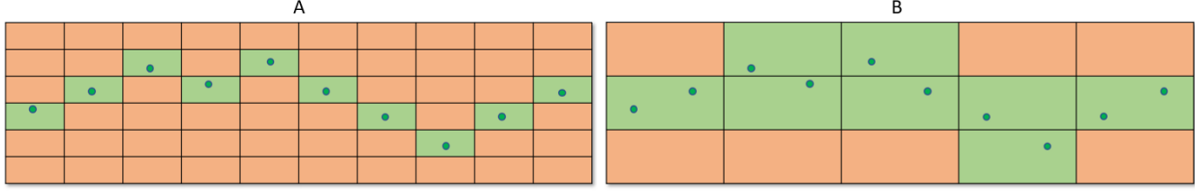

Figure 7: A two dimensional example of the box counting method used to determine fractal dimension. In Figure 7a, $s_i = 1$, $N(s_i) = 10$ and in Figure 7b $s_i = 2$, $N(s_i) = 8$ demonstrating the expected relationship between the two variables.

To determine D to a high accuracy, a minimum of five data points were required to fit with Equation 11. For low roughness values, cube sizes of less than one were necessary. The rough terrain formed by the DSA was in the form of a two dimensional array grid in X and Y, with the bacteria heights as Z. Although it was initially unclear how to count using box sizes of less than one along X, Y, this issue was solved by scaling the array in X and Y by ten. The algorithm then sampled this modified array using boxes of length [1, 1, 0.1], equivalent to sampling the original array using a box of side length 0.1. To determine fractal dimension, the sampling cubes used were of side length: 0.4, 0.8, 1.6, 3.2 and 6.4 μm.

4   Results and discussion

4.1   Diffusion through Simple Shapes

Initially, biofilms of simple shapes were investigated within the simulation. This included spherical, hemispherical and two cylindrical biofilms.
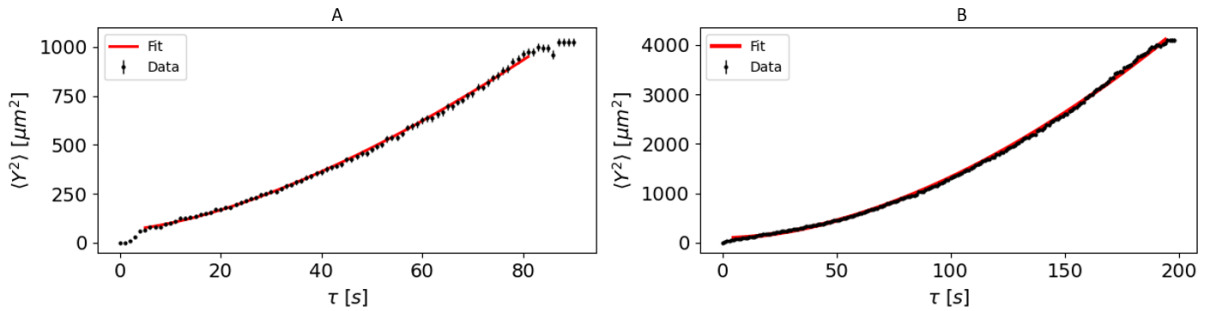

Figure 8: *A* shows a plot of wavefront position squared over time for the sphere and *B* shows the same relationship for a cylinder (with the two flat faces of the cylinder on the simulation boundaries). Five repeats were taken for each shape which formed the dominant uncertainty. The reduced chi-squared values were 0.46 and 2.07 for the sphere and cylinder respectively. This demonstrates the data was in accordance with the fitting equation applied given the uncertainty estimates.

As shown in Figure 8, not all of the data points were fit. The region to be fit was chosen to exclude diffusion at the very start and end of the waves propagation. At the start, there appears a

characteristic critical volume below which the wave cannot propagate within the bacteria. The diffusion of K^+ here was a consequence of the initial spike and not the bacteria firing, hence it does not help us understand the communication properties within the bacteria. A critical radius was found using the constant fitting term as an approximation for the length scale over which the biofilm must be before the wave propagates. A weighted average of these across the four simple shapes gives a critical radius of $8.49 \pm 0.76 \, \mu$m leading to a critical volume of $2560 \pm 690 \, \mu$m^3. At the end of the waves propagation, it reaches the edge of the bacteria and hence this is also not a region of interest for the study. In both of these regions, normal diffusion is observed in which $\alpha \approx 1$.

Shape	α
Sphere	1.54 ± 0.01
Hemisphere	1.69 ± 0.02
Cylinder (Far Boundary)	1.78 ± 0.01
Cylinder (Tight Boundary)	1.76 ± 0.01

Table 1: Diffusion exponent, α, for all simple shapes considered in the study.

K^+ waves were seen to show superdiffusive time-scaling as per Equation 9 within all simple shapes. This is to be expected given the active firing mechanism of the bacteria which acts to accelerate the wave through the biofilm, increasing the diffusion exponent.
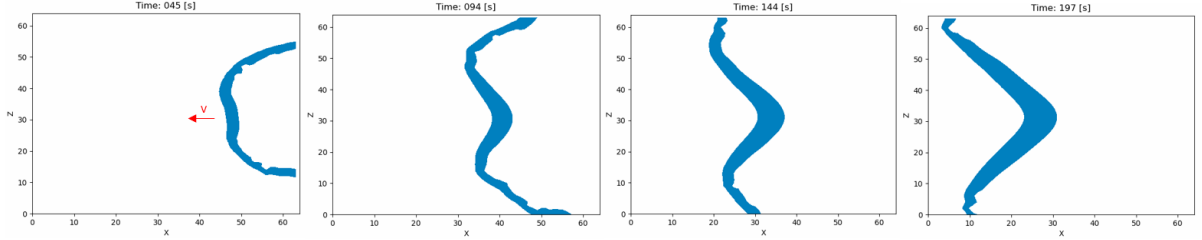

Figure 9: Position of the K^+ wavefront propagating through a cylinder with tight boundaries at four different instances in time. The red arrow indicates the direction of wave propagation through the cylinder and reflective boundaries are set along $Z = 0$ and $Z = 64$. Images show a cross-section taken through the central axis of the cylinder.

As observed in Figure 9, there was a significant increase in wave propagation speed along the reflective boundaries of the simulation. For bacteria close to these boundaries, a waves energy would no longer decay according to the typical inverse-square law. Some potassium which may have fired bacteria at greater radial distances is reflected inwards resulting in a higher wave velocity along these boundaries as bacteria is fired earlier. This effect may be used to explain the diffusion exponents of the simple shapes. The lowest diffusive exponent, observed within the sphere, did not have any of its faces on a reflective boundary.

13

4.2 Diffusion around a Channel

Both a circular hole through a cylinder and a square hole through the center of a cube were considered during the study. This was not only analysed as channels are observed within many biofilms, but because a greater understanding of the way holes impede biofilm communication may aid the development of new technology which can weaken the cooperation within unwanted biofilms.
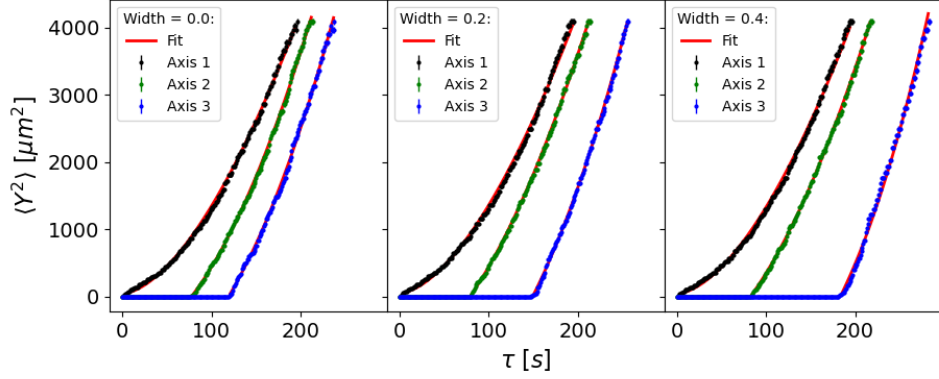

Figure 10: Diffusion properties for K^+ propagating within cylinders of varying hole size. A hole of width W implies W is equal to the diameter of the hole divided by the diameter of the bottom face of the cylinder. Axis 1 is an axis parallel to the central axis but 3 μm from the edge of the cylinder. Axis 2 and 3 represent rotations of Axis 1 about the central axis by 90° and 180° respectively, as shown in Figure 4B. The cylinder was of length and diameter 64 μm.

To investigate the effect a hole has on the propagation of the wave, the MFPT of the wave between the initial spike on the bottom face (Axis 1) to positions on the opposite face was recorded. The increase in time required to communicate with bacteria along Axis 2 or Axis 3 on the opposite face when a circular hole is introduced was then analysed. Bacteria on Axis 3 have a greater MFPT when a larger width hole is introduced through the center of the cylinder. The resulting time delay can be attributed to two sources: an increase in the minimum propagation distance of the wave (assuming propagation through only bacteria dense regions) and a decrease in the average wave velocity as its spherical symmetry is broken. These time delays are denoted by Δt_1 and Δt_2 respectively. Therefore, the total time delay created by the addition of a hole in the biofilm is $\Delta t_{tot} = \Delta t_1 + \Delta t_2$, where Δt_{tot} is obtained from the simulation.

To calculate the significance of both effects, the change in minimum propagation distance (MPD) due to the introduction of a hole must be determined. When the wave propagated to bacteria along Axis 2 on the opposite face, only circular holes of $W > 0.64$ increased this distance. As a consequence, for waves travelling to Axis 2, $\Delta t_1 = 0$. This meant delays of $\Delta t_2 = (1.00 \pm 2.89)$s and $\Delta t_2 = (5.63 \pm 4.39)$s for holes of width $W = 0.2$ and $W = 0.4$ respectively. These results indicate there is a negligible time-delay for communication around one quarter of a circular hole if it does not directly change the MPD. For communication to bacteria along Axis 3 on the opposite face of the cylinder, the introduction of a circular hole resulted in a MPD for the wave of $\sqrt{64^2 + 4(29^2 + (32W)^2)}\,\mu$m. These results were compared to the communication between bacteria in opposite corners of a cuboidal biofilm with a square hole through one axis. Within this biofilm, the MPD was $64\sqrt{1 + (1+W)^2 + (1-W)^2}\,\mu$m.
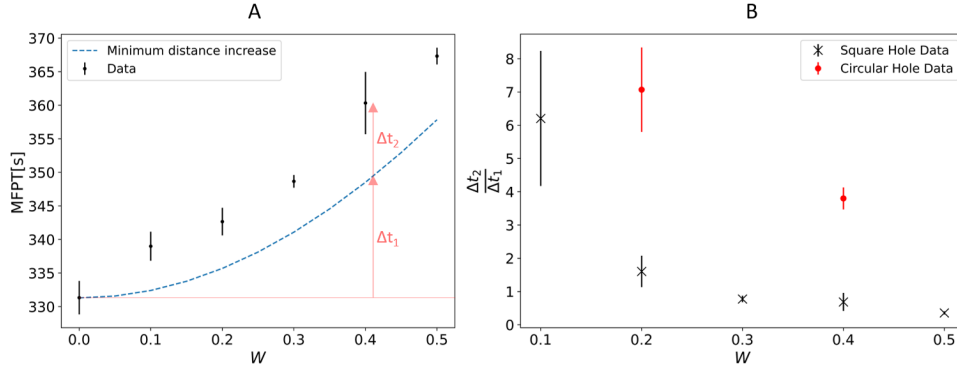
Figure 11: *A* shows MFPT against *W*, for a cuboidal biofilm of side length 64 μm with a square through one axis. The line labelled 'Minimum distance increase' represents the MFPT if the same average velocity was observed for all hole widths and is a result of a change in MPD. *B* is the ratio between the two delay effects plotted against hole width for biofilms with circular and square holes.

Shown by Figure 11B, the dominant delay effect for communication across both hole shapes was the break in symmetry of the wave for small hole widths of $W < 0.3$ and an increase in propagation distance caused by large hole widths when $W > 0.3$. Figure 11 therefore indicates that a small hole of either shape is adequate to break the propagating waves symmetry and cause a significant delay to communication across a biofilm.

The dominant error in Figure 11B is from the error on Δt_{tot} which is propagated to Δt_2. This arises from the random generation of bacteria positions within both biofilm geometries and was quantified by taking the deviation in three repeats for each MFPT. Hence, the reason the data point for the square hole of width $W = 0.1$ has a high uncertainty is because it has the highest fractional uncertainty for Δt_2 given the value itself is low and the uncertainty is approximately constant. A minor uncertainty on Δt_1 was also considered. This originated from an uncertainty in the average velocity of the wave when no hole was present. This velocity was used to calculate the expected time delay due to an increase in MPD, resulting in an error on Δt_1. This was estimated using the uncertainty in MFPT when no hole was present.

The data also suggests that the introduction of a circular hole causes a greater delay through the distortion to the symmetry of the propagating wave than a square hole. More than two hole widths are required to confidently claim this statement so further investigation into this is required to check the hypothesis. The above findings may mean the control of unwanted biofilms through the disruption of their communication mechanisms could be aided through the introduction of smaller holes than one might expect.

4.3 Diffusion across a Fractal Surface

During this section of the study, the DSA was used to form rough surface of dimensions 129 by 129 μm. A bacteria at the middle of one edge of the surface was spiked and the MFPT of the wavefront was measured on the opposite side of the terrain.
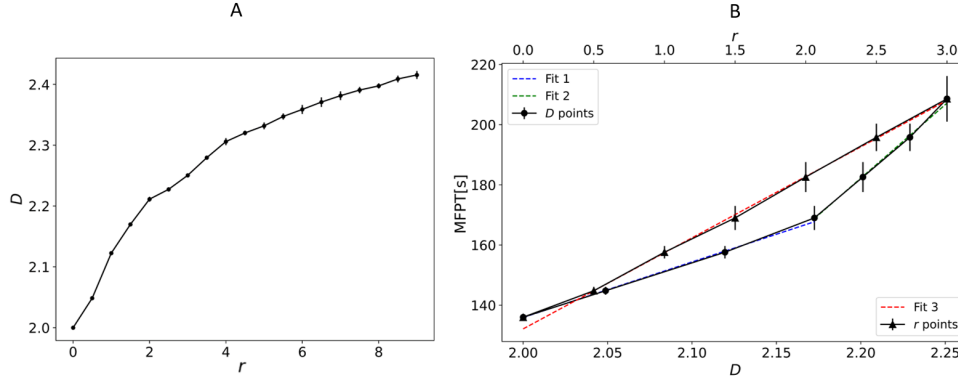
Figure 12: *A* shows the fractal dimension of the terrain generated, found using the box counting method, against the roughness parameter *r*. *B* shows a linear relationship between MFPT and DSA surface roughness parameter and two different linear fits for different fractal dimensions within the MFPT against fractal dimension plot. All DSA results were found using five repeats for each surface roughness.

MFPT was found to be directly proportional to surface roughness, *r*, where MFPT increased by (25.3 ± 0.1)s per unit roughness. The average difference in height between adjacent bacteria increases proportionally to *r*. This is demonstrated in Appendix A.2 in which R_{rms}, the average deviation between the height of adjacent bacteria, is plotted against *r*. This means that a linear relationship between MFPT and *r* is initially counter-intuitive. The average distance between adjacent bacteria would increase at a rate that was less than proportional to the average height difference between bacteria. Hence, it may be expected that Fit 3 on Figure 12B was of the form MFPT $\propto r^x$ where $x > 1$. The MFPTs correlation to *r* may be better explained here by considering the fact the first-passing wave on the opposite side of the surface may travel a shorter distance than simply via straight lines between adjacent bacteria. The wave may sooner reach the opposite side of the terrain by propagating across the plane of the surface, travelling around bacteria with large deviations in height to the current wave height. This would lower the MFPT and may explain the observed linearity.

Using the relationship between fractal dimension and surface roughness in Figure 12A, MFPT was found to increase with fractal dimension for $D < 2.17$ at (184.4 ± 4.2)s per unit dimension and for $D > 2.17$ at (488.7 ± 15.1)s per unit dimension. This demonstrates that a biofilm may have some optimum fractal dimension in the region of $D \approx 2.17$ which maximises the ratio between surface area (allowing the biofilm maximum uptake of surrounding nutrients) to MFPT. Further investigation into the relationship between surface area and fractal dimension, as well as a greater number of data points demonstrating the above step change in gradient, would be required to confidently make such an assertion as this region may become a smoother transition with more data.

The maximum fractal dimension generated by the DSA tends to 2.45, above which increasing *r* has a negligible effect. If the study was to be extended, a fractal generator that formed self-similar shapes in all three dimensions, rather than one that forms surfaces by variation in one dimension, may be implemented to investigate the biomass of a biofilm rather than the surface. To model a biofilm surface more accurately, the DSA could be improved to define a surface under which bacteria are randomly spawned, reflecting the random nature of biofilm formation.

An inverse relationship between R_{ku} and *r* was found for the DSA terrains. Leptokurtic kurtosis

was found for $r < 1$ and platykurtic kurtosis for $r > 1$. A brief discussion of this, and an example DSA height distribution, is included in Appendix A.2.

During the final section of the study, both 2D and 3D Menger sponges were investigated. A 3D Menger sponge with holes through only one axis (rather than all three axis as in the typical 3D Menger) was also included. For both of the 3D Menger sponges, a bacteria was spiked at one corner of the biofilm and the MFPT to the opposite corner was recorded. For the 2D Menger, the MFPT was taken in the same manner as the DSA surfaces. The bacteria spacing was kept constant for all the fractals (including the DSA surfaces) at $2\,\mu m$ and a side length of $52\,\mu m$ was used for all fractals except the DSA terrains.
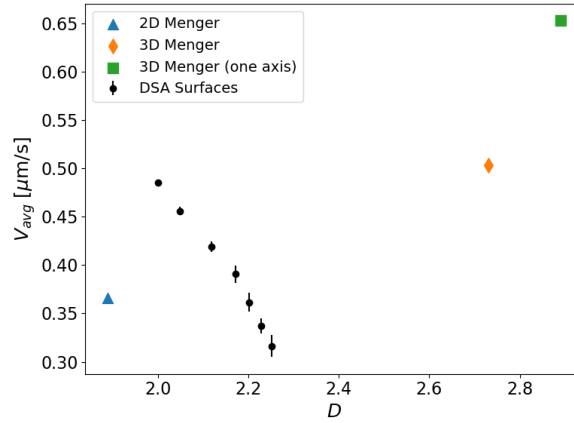

Figure 13: A plot of average velocity, V_{avg} against D for all fractals considered within the study. Only uncertainties for the DSA terrains are included as all the other fractals were formed with definitive bacteria positions. First-passage times were 142 s, 138 s and 179 s for the 2D Menger, 3D Menger and 3D Menger with holes through one axis respectively.

Figure 13 shows an increasing relationship between average velocity and fractal dimension with the exception of the DSA terrains. It is worthwhile noting that there are a range of different bacteria geometries that may form shapes of similar fractal dimension. It is also important that, in the same way a flat shape has a Minkowski-Bouligand dimension $D = 2$ by having a full plane of evenly spaced bacteria, a shape formed across three Cartesian dimensions has $D = 3$ if it is a uniform cube of evenly spaced bacteria. This means that one may expect a positive correlation between V_{avg}, which increases with bacteria density, and D. Therefore, it is likely there are other features of a biofilm which more directly affect electro-signalling properties such as the typical spacing between bacteria and any interruption to the spherical symmetry of the wave introduced by irregularities in the bacteria density. A positive correlation between fractal dimension and wave velocity is therefore likely a secondary effect of more direct features of the biofilm which impact long-range communication.

5 Conclusion

With such a significant array of chronic and reoccuring health problems stemming from bacterial biofilms, a deeper understanding of their long-range communication mechanism is an important step in the persuit toward better control of biofilm-mediated drug resistance and improved methods for dispersal agent delivery. Consequently, this study aimed to investigate the effects of shape, fractal dimension and channels on electro-signalling in biofilms.

Potassium waves propagating through cuboidal, hemispherical and spherical biofilms were all seen to follow a superdiffusive time-scaling as predicted by anomalous diffusion theory. A universal relationship between fractal dimension and the speed of communication through a biofilm was not identified, likely due to factors such as bacteria density and biofilm shape which play a more direct role in the signalling properties of biofilms. However, the mean first passage time across a rough surface was shown to be proportional to a conventional surface roughness parameter, the route-mean-square of the bacteria heights. Lastly, both square and circular holes through one axis of a biofilm were shown to significantly delay communication. This was not only due to an increase in minimum propagation distance between bacteria, but due to a disruption in the spherical symmetry of the propagating wave.

Potential further studies, which work towards more physical biofilm models, may introduce the inclusion of the Hodgkin-Huxley equations within current ABMs. Through further investigation into the way in which channels and surface roughness may delay communication around a biofilm, one would hope this may lead to new methods aimed at limiting electro-signalling within unwanted biofilms and ultimately save lives.

References

[1] T. Beveridge *et al*. Interactions between biofilms and the environment. *FEMS Microbiology Reviews*, 20(3-4):291–303, 1997.

[2] D. Lopez, H. Vlamakis, R. Kolter. Biofilms. *Cold Spring Harb Perspect Biol.*, 2(7), 2010.

[3] R. Donlan. Biofilms: Microbial life on surfaces. *Emerging Infectious Diseases*, 8(9), 2002.

[4] H. Flemming *et al*. *Biofilms: Recent Advances in their Study and Control*, chapter 2, page 19. Harwood Academic Publishers, 2005.

[5] K. Lewis. Riddle of biofilm resistance. *Antimicrobial Agents and Chemotherapy*, 45(4):999–1007, 2001.

[6] R.D. Wolcott *et al*. Chronic wounds and the medical biofilm paradigm. *Journal of Wound Care*, 19(2):45–53, 2010.

[7] L. Rooney *et al*. Intra-colony channels in e. coli function as a nutrient uptake system. *The ISME Journal*, 14(10):2461–2473, 2020.

[8] C. Solano, M. Echeverz, I. Lasa,. Biofilm dispersion and quorum sensing. *Current Opinion in Microbiology*, 18:96–104, 2014.

[9] S. Manna *et al*. Electrochemical communication in biofilm of bacterial community. *J. Basic Microbiol.*, 60(10):819–827, 2020.

[10] J. Keener, J. Sneyd. *Mathematical Physiology*. Springer New York, 2009.

[11] G.V. Petkov. Ion channels. In *Pharmacology*, pages 387–427. Elsevier, 2009.

[12] A. Prindle *et al*. Ion channels enable electrical communication in bacterial communities. *Nature*, 527(7576):59–63, 2015.

[13] J. Liu *et al.* Metabolic co-dependence gives rise to collective oscillations within biofilms. *Nature*, 523(7562):550–554, 2015.

[14] W. Epstein. The roles and regulation of potassium in bacteria. In *Progress in Nucleic Acid Research and Molecular Biology*, pages 293–320. Elsevier, 2003.

[15] A. Fick. V. on liquid diffusion. *The London, Edinburgh, and Dublin Philosophical Magazine and Journal of Science*, 10(63):30–39, 1855.

[16] A. Einstein. Über die von der molekularkinetischen theorie der wärme geforderte bewegung von in ruhenden flüssigkeiten suspendierten teilchen. *Annalen der Physik*, 322(8):549–560, 1905.

[17] J.Klafter, I.M Sokolov. Anomalous diffusion spreads its wings. *Physics World*, 18(8):29–32, 2005.

[18] M.J. Saxton. A biological interpretation of transient anomalous subdiffusion. i. qualitative model. *Biophysical Journal*, 92(4):1178–1191, 2007.

[19] J.F. Reverey *et al.* Superdiffusion dominates intracellular particle motion in the supercrowded cytoplasm of pathogenic *Acanthamoeba castellanii*. *Scientific Reports*, 5(1), 2015.

[20] M. Peccianti, R. Morandotti. Beyond ballistic. *Nature Physics*, 8(12):858–859, 2012.

[21] B. Mandelbrot. How long is the coast of britain? statistical self-similarity and fractional dimension. *Science*, 156(3775):636–638, 1967.

[22] Y. Jin *et al.* Definition of fractal topography to essential understanding of scale-invariance. *Scientific Reports*, 7(1), 2017.

[23] X. Wang, F. Becker, P. Gascoyne. The fractal dimension of cell membrane correlates with its capacitance: A new fractal single-shell model. *Chaos: An Interdisciplinary Journal of Nonlinear Science*, 20(4):043133, 2010.

[24] S. J. Robbins. The fractal nature of planetary landforms and implications to geologic mapping. *Earth and Space Science*, 5(5):211–220, 2018.

[25] P. Pfeifer. Fractal dimension as working tool for surface-roughness problems. *Applications of Surface Science*, 18(1-2):146–164, 1984.

[26] M. Minsky. Memoir on inventing the confocal scanning microscope. *Scanning*, 10(4):128–138, 1988.

[27] L. A. Trinh, S. E. Fraser. Chapter twenty-one - imaging the cell and molecular dynamics of craniofacial development: Challenges and new opportunities in imaging developmental tissue patterning. volume 115 of *Current Topics in Developmental Biology*, pages 599–629. Academic Press, 2015.

[28] A. Martínez-Calvo *et al.* Morphological instability and roughening of growing 3d bacterial colonies. *Proceedings of the National Academy of Sciences*, 119(43), 2022.

[29] S.W. Hermanowicz, U. Schindler, P. Wilderer. Anisotropic morphology and fractal dimensions of biofilms. *Water Research*, 30(3):753–755, 1996.

[30] W. Zahid, J. Ganczarczyk. A technique for a characterization of rbc biofilm surface. *Water Research*, 28(10):2229–2231, 1994.

[31] A. Matyjaszkiewicz *et al.* BSim 2.0: An advanced agent-based cell simulator. *ACS Synthetic Biology*, 6(10):1969–1972, 2017.

[32] M. Sidortsov, Y. Morgenstern, A. Be'er. Role of tumbling in bacterial swarming. *Physical Review E*, 96(2), 2017.

[33] M. Frame B. Mandelbrot. Fractals. In Robert A. Meyers, editor, *Encyclopedia of Physical Science and Technology (Third Edition)*, pages 185–207. Academic Press, 2003.

[34] L.Carpenter A. Fournier, D.Fussell. Computer rendering of stochastic models. *Communications of the ACM*, 25(6):371–384, 1982.

[35] G. Guido. A practical implementation of the box counting algorithm. *Computers Geosciences*, 24(1):95–100, 1998.

A   Appendix

A.1   Initial Parameters

As mentioned in Section 3.3, a table of initial parameters used within the model is included here.

Parameter	Value
D_K	$1 \times 10^{-1}\ \mu\text{m}^2\text{s}^{-1}$
σ	$5 \times 10^9\ \mu\text{m}^{-3}$
k	$1 \times 10^{-5}\ \text{s}^{-1}$
σ^*	$3 \times 10^8\ \mu\text{m}^{-3}$
$totbac$	6×10^3

Table 2: Table of initial parameters. The motivations for these values are explained in Section 3.3. $totbac$ is the total bacteria for a spherical biofilm of radius $64\ \mu$m leading to a uniform bacteria density of $3.11 \times 10^{-4}\ \mu\text{m}^{-3}$. This was maintained throughout all simple shapes.

A.2   Diamond-Square Algorithm Distribution

The distribution of bacteria heights generated by the DSA was also investigated during the study.
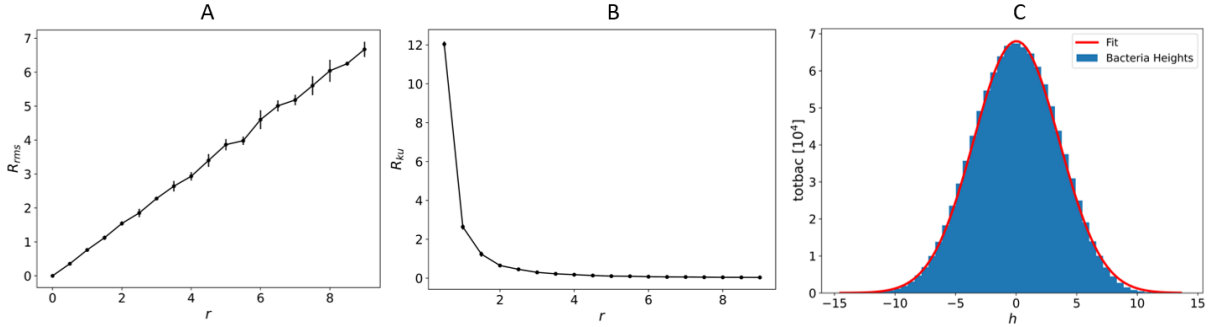

Figure 14: *A* shows the linear relationship between R_{rms} (the standard deviation) of the bacteria heights generated by the DSA and r. *B* demonstrates the inverse relationship between the distributions kurtosis and r. *C* shows the distribution of bacteria heights fit with a Gaussian curve for $r = 3$.

The distribution of bacteria heights for all physical r generated during the study followed Gaussian distributions, with means $\mu \approx 0$ and standard deviations, $\sigma \propto r$. Leptokurtic kurtosis ($R_{ku} > 3$) is observed for $r < 1$ in which the outlier frequency is high. The very low deviations in bacteria heights means that any significant variation in height from the mean of zero increases the kurtosis significantly. To contrast, the kurtosis is lower than that of a normal distribution for increasing r and so platykurtic kurtosis is observed ($R_{ku} < 3$) for $r > 1$. This is a positive feature of the DSA as in the case of physical biofilms bacteria tend to form in tight clusters where large outliers are rare.